Research Square

Preprints are preliminary reports that have not undergone peer review.
They should not be considered conclusive, used to inform clinical practice,
or referenced by the media as validated information.

Photocatalytic degradation of tetracycline hydrochloride using g-C_3N_4/CdS composites

Tianyu Zhou
Shaanxi University of Technology
Jianping Deng
jpdeng0214@snut.edu.cn
Shaanxi University of Technology
Liang Li
Shaanxi University of Technology
Mingtong Nie
Shaanxi University of Technology
Junfei Fang
Shaanxi University of Technology
Rui Feng
Shaanxi University of Technology

Research Article

Keywords: g-C_3N_4, CdS, heterojunction, tetracycline hydrochloride, visible-light photocatalysis, charge-carrier separation

Posted Date: November 25th, 2026

DOI: https://doi.org/10.21203/rs.3.rs-11498265/v1

License: This work is licensed under a Creative Commons Attribution 4.0 International License.
Read Full License

Additional Declarations: No competing interests reported.

Photocatalytic degradation of tetracycline hydrochloride using g-C_3N_4/CdS composites

Tianyu Zhou [a†], Jianping Deng [a b*], Liang Li [a], Mingtong Ni [a], Junfei Fang [a], Rui Feng [a]

[a] School of Mechanical Engineering, Shaanxi University of Technology, Hanzhong 723001, China
[b] School of Physics and Telecommunication Engineering, Shaanxi University of Technology, Hanzhong 723001, China

Email addresses: Tianyu Zhou, 494779573@qq.com; Jianping Deng, jpdeng0214@snut.edu.cn; Liang Li, m18628405286@163.com; Mingtong Ni, 19894701475@163.com; Rui Feng, 17730784553@163.com; Junfei Fang, jffang@snut.edu.cn

*Corresponding Author: jpdeng0214@snut.edu.cn
† Joint first authors

ABSTRACT

Rapid carrier recombination and slow interfacial charge transport restrict the visible-light photocatalytic activity of graphitic carbon nitride (g-C_3N_4). Prepared by one-step high-temperature calcination, g-C_3N_4 served as the substrate for in situ hydrothermal CdS growth. The resulting composites, with nominal CdS contents of 3%, 6%, 9%, and 12%, were tested for tetracycline hydrochloride (TCH) degradation under visible light. Characterization by XRD, SEM, EDS, XPS, UV–Vis spectroscopy, PL, EIS, transient photocurrent, CV, and Mott–Schottky measurements covered the crystal phases, morphology, surface chemical states, absorption, and photogenerated charge behavior. CdS particles were distributed over the g-C_3N_4 sheets, and the characteristic phases of g-C_3N_4 and hexagonal wurtzite CdS remained present. Among the loading series, the 9% composite had the weakest PL emission, highest transient photocurrent, and smallest EIS arc. These responses support improved carrier separation and interfacial charge transfer. Hydrothermal-temperature optimization gave the highest degradation rate for the 9% sample prepared at 140 °C, with an apparent first-order rate constant of 0.02508 min^{-1}. Reuse largely preserved its principal crystalline phases, and the highest degradation efficiency occurred at pH 7. Scavenger tests indicated that $\cdot O_2^-$ and h^+ dominated the reaction, with a secondary contribution from ·OH. The results associate the improved performance with CdS loading and hydrothermal temperature through their effects on interfacial structure and charge behavior, supporting visible-light treatment of antibiotic-containing wastewater with g-C_3N_4/CdS.

KEYWORDS: g-C_3N_4 ,CdS, heterojunction, tetracycline hydrochloride, visible-light photocatalysis, charge-carrier separation

1. INTRODUCTION

Incomplete removal during conventional treatment allows antibiotic residues to enter surface water, groundwater, and wastewater-treatment systems continuously. Tetracycline hydrochloride (TCH), used to prevent and treat diseases in humans and livestock, is one such pollutant. Its water solubility, stable polycyclic structure, and mobility favor persistence in aquatic environments. Tetracyclines in these environments are also associated with the distribution of antibiotic-resistance genes. In water-source samples from the Wuhan reach of the Yangtze River, the maximum reported tetracycline concentration was 1708.33 ng/L. This observation points to risks for drinking-water sources and aquatic ecosystems [1].

Aquatic organisms can be affected directly by TCH discharged into water. Prolonged exposure, even at low concentrations, may change microbial-community structure and increase selection pressure for antibiotic-resistance genes. Degradation does not necessarily remove the ecological risk: tetracycline intermediates may be as harmful as the parent compound or more so. A decrease in TCH concentration therefore provides only part of the assessment of treatment performance. The extent of oxidation, the reactive species involved, and the ecological risks of transformation products also need to be considered [2].

Antibiotic-containing wastewater has been treated by adsorption, membrane separation, coagulation–sedimentation, and biological processes. Pollutant transfer, membrane fouling, long treatment times, and incomplete degradation limit the practical use of these approaches. Photocatalytic oxidation provides another route. When a semiconductor absorbs light, the generated electrons and holes can produce reactive oxygen species that attack aromatic rings, amide groups, and conjugated structures in antibiotic molecules. These reactions promote degradation of persistent pharmaceutical pollutants.

Visible-light response, chemical stability, metal-free composition, and straightforward preparation make graphitic carbon nitride (g-C_3N_4) an attractive semiconductor photocatalyst. Its bulk form has several drawbacks. A limited specific surface area and pronounced interlayer stacking accompany inadequate visible-light utilization and rapid electron–hole recombination, restricting photocatalytic activity. Joint regulation of carbon and nitrogen vacancies reportedly improves carrier separation and visible-light TCH degradation in g-C_3N_4 [3].

A semiconductor with compatible band positions can complement g-C_3N_4 when the two are coupled. The relatively narrow band gap of CdS gives it strong visible-light absorption, while close CdS/g-C_3N_4 contact can provide a route for photogenerated carriers. These properties make CdS a

useful coupling partner. CdS also undergoes rapid electron–hole recombination and is susceptible to photocorrosion, however. Composite performance consequently depends on how much CdS is present, how the particles disperse, and how closely the phases contact one another.

Several studies have demonstrated efficient antibiotic degradation with g-C_3N_4/CdS composites. In the CdS/square-tubular g-C_3N_4 heterojunction reported by Jing et al., improved carrier separation and migration enabled both H_2O_2 production and tetracycline degradation [4]. Feng et al. coupled tetracycline degradation with Cr(VI) reduction using a Cd/CdS/g-C_3N_4 interface [5]. For peroxymonosulfate activation and tetracycline degradation, Zhang et al. constructed a g-C_3N_4/CdS heterojunction in situ [6]. Effective removal of tetracycline and ciprofloxacin under sunlight has also been reported for surface-modified g-C_3N_4/CdS composites [7]. These examples link interface design to improvements in the photocatalytic behavior of g-C_3N_4/CdS.

CdS addition has an optimum range. Low contents leave few effective heterointerfaces, while excessive loading can cover active sites, shield light, aggregate particles, and introduce carrier-recombination centers. Increasing CdS content therefore does not produce a continuous gain in photocatalytic performance. Selecting a suitable proportion requires examining how composition affects crystal structure, interfacial charge behavior, and TCH degradation. XRD, XPS, UV–Vis DRS, PL, EIS, transient photocurrent, and CV measurements must be interpreted together to establish those relationships.

This study compared pure g-C_3N_4 and pure CdS with g-C_3N_4/CdS composites containing nominally 3%, 6%, 9%, and 12% CdS for TCH degradation under visible light. Heterointerface formation, optical response, and the separation and transport of photogenerated carriers were examined by XRD, SEM, XPS, UV–Vis DRS, PL, EIS, transient photocurrent, CV, and Mott–Schottky measurements. Degradation tests also covered initial TCH concentration and solution pH. Scavenger experiments were then used to identify the main reactive species.

2. EXPERIMENTAL SECTION

2.1 Preparation of g-C_3N_4

Thermal polymerization was used to prepare g-C_3N_4. A covered 100 mL crucible containing 15 g of urea was wrapped tightly in aluminum foil to limit precursor loss on heating. It was placed in a muffle furnace and held at 550 °C for 3 h. The furnace cooled naturally to room temperature before the bulk product was collected.

After cooling, the product was ground and washed by centrifugation to remove residual urea and soluble impurities. Absolute ethanol and deionized water were used alternately, with three washes in each solvent. Drying at 60 °C for 8 h and a second grinding step yielded pale-yellow g-

C_3N_4 powder, which was sealed for storage. The calcination process converts urea into conjugated graphitic carbon nitride through condensation and deamination [8].

2.2 Preparation of g-C_3N_4/CdS composites with different CdS loadings

Scheme 1 outlines the in situ hydrothermal synthesis of g-C_3N_4/CdS. Nominal CdS proportions of 3%, 6%, 9%, and 12% were used to prepare samples designated g-C_3N_4/CdS (3%), g-C_3N_4/CdS (6%), g-C_3N_4/CdS (9%), and g-C_3N_4/CdS (12%), respectively. Each preparation contained 0.92 g of g-C_3N_4, 50 mL of deionized water, and 0.05 g of sodium dodecylbenzenesulfonate (SDBS). The cadmium and sulfur precursor amounts were the only quantities varied across this series.

A suspension of 0.92 g of g-C_3N_4 in 50 mL of deionized water was dispersed by magnetic stirring and ultrasonication for 30 min. After adding 0.05 g of SDBS, stirring continued for 30 min. SDBS improved the wettability and dispersion stability of g-C_3N_4 and helped Cd^{2+} adsorb uniformly on its surface.

The suspension pH was adjusted to 8–10 by dropwise addition of dilute aqueous ammonia, after which cadmium nitrate tetrahydrate solution was introduced. The $Cd(NO_3)_2 \cdot 4H_2O$ amounts were 0.09255, 0.18510, 0.27765, and 0.37020 g for the 3%, 6%, 9%, and 12% samples, respectively. Continuous stirring was maintained for 90 min after the cadmium precursor had been added.

Thiourea supplied the sulfur for CdS formation. For the 3%, 6%, 9%, and 12% samples, 0.00990, 0.01980, 0.02970, and 0.03960 g were added, respectively, followed by another 30 min of stirring. Under hydrothermal conditions, the sulfur-containing species released from thiourea react with Cd^{2+} to produce CdS nanocrystals. Nucleation and growth on the g-C_3N_4 surface bring the two phases into close interfacial contact [4–6].

Hydrothermal treatment was carried out in a polytetrafluoroethylene-lined autoclave at 140 °C for 300 min. Once the suspension had cooled naturally to room temperature, the product was recovered by centrifugation. Alternating washes with deionized water and absolute ethanol were repeated three times for each solvent. The recovered material was dried at 80 °C until its mass was constant and then ground to yield the g-C_3N_4/CdS samples.

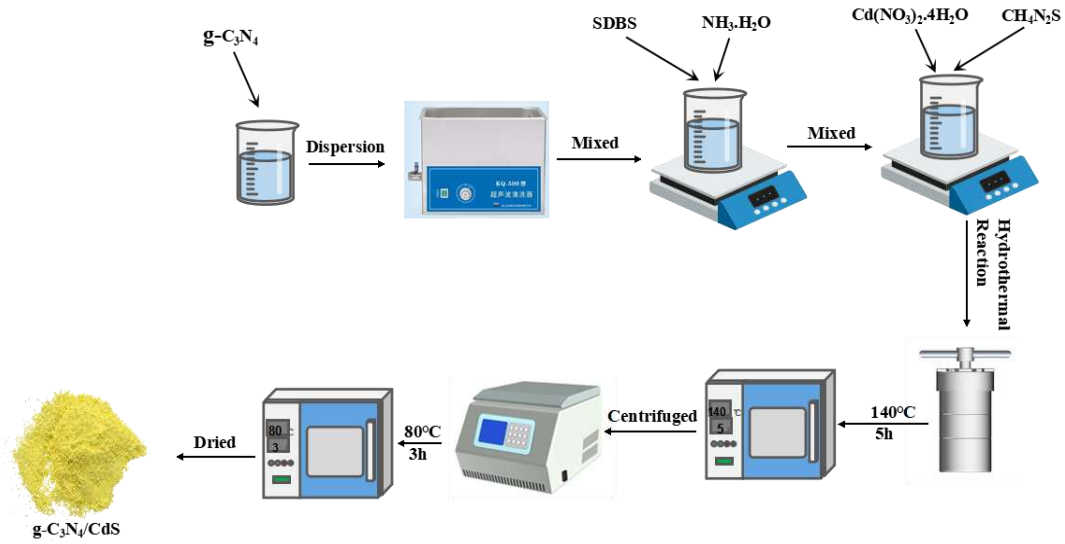

Scheme 1. Schematic illustration of the preparation of g-C_3N_4/CdS composites.

2.3 Materials characterization

Crystal phases and surface morphology were examined by X-ray diffraction (XRD) and scanning electron microscopy (SEM), respectively, with SEM also revealing interfacial dispersion. X-ray photoelectron spectroscopy (XPS) measured the surface elemental composition and chemical states. Ultraviolet–visible diffuse-reflectance spectroscopy (UV–Vis DRS) assessed absorption and provided optical band-gap estimates. Photoluminescence (PL) spectroscopy probed carrier recombination. For the illuminated samples, electrochemical impedance spectroscopy (EIS) and transient photocurrent measurements assessed interfacial charge-transfer resistance and carrier separation and transport. Cyclic voltammetry (CV) added a comparison of electrochemical redox responses. Mott–Schottky measurements identified semiconductor type and estimated flat-band potentials, which were combined with the optical band gaps to assess band alignment. BET and FTIR measurements were not performed.

2.4 Photocatalytic degradation tests

Visible-light photocatalytic activity was tested with tetracycline hydrochloride (TCH) as the target pollutant. Each typical run used 0.05 g of catalyst suspended in 100 mL of 50 mg L^{-1} TCH solution. Before exposure to a 20 W LED lamp, the suspension was stirred in darkness for 30 min to reach adsorption–desorption equilibrium. Samples were taken at 15 min intervals during irradiation and centrifuged to separate the catalyst. UV–Vis measurements of the supernatant at 357 nm were converted to TCH concentrations using the calibration curve.

Calibration began with UV–Vis absorption spectra of TCH standards at 10, 20, 30, 40, and 50 mg L^{-1}. Two characteristic peaks appeared near 276 and 357 nm. Absorbance at 357 nm was used

to obtain the linear calibration equation and its coefficient of determination (R^2). Pure g-C_3N_4, pure CdS, and the 3%, 6%, 9%, and 12% g-C_3N_4/CdS composites were then tested under the same reaction conditions. Subsequent initial-concentration and pH tests used the 9% sample. Residual TCH concentration is expressed as C_t/C_0, and Eq. (1) was used to calculate degradation efficiency.

$$R(\%) = \left(1 - \frac{C_t}{C_0}\right) \times 100\% \quad (1)$$

where R denotes TCH degradation efficiency (%), C_0 denotes the initial solution concentration (mg L^{-1}), and C_t denotes the TCH concentration (mg L^{-1}) at irradiation time t. The irradiation time t is expressed in min.

3. RESULTS AND DISCUSSION

3.1 Crystal structure analysis by XRD

In Fig. 2, the XRD patterns compare pure g-C_3N_4 and pure CdS with the composites containing 3%, 6%, 9%, and 12% CdS. The characteristic peaks of pure g-C_3N_4 occur at 2θ ≈ 13.1° and 27.4° and correspond to the (100) and (002) planes. In-plane periodic ordering of triazine units gives the weak peak at 13.1°. Periodic stacking of conjugated aromatic layers accounts for the stronger reflection at 27.4° [8].

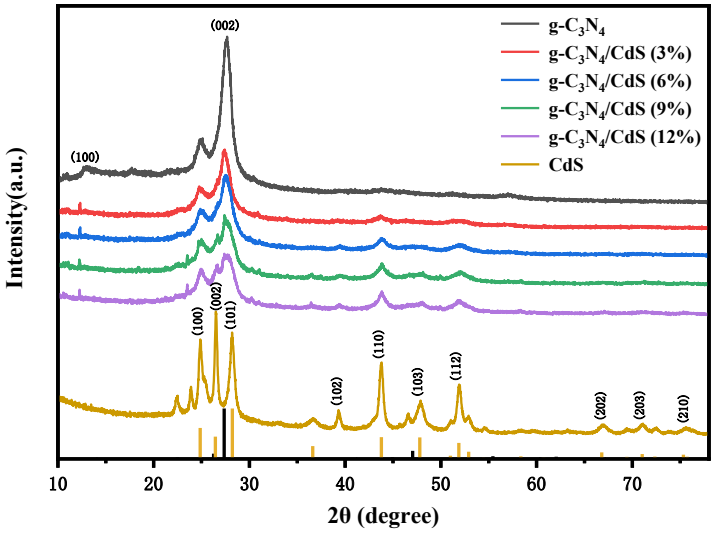

Fig. 2. XRD patterns of pure g-C_3N_4, g-C_3N_4/CdS composites with different CdS proportions, and pure CdS.

The diffraction peaks of pure CdS occur at 2θ ≈ 24.8°, 26.5°, 28.2°, 36.6°, 43.7°, 47.8°, and 51.8°. Their assignment to the (100), (002), (101), (102), (110), (103), and (112) planes matches hexagonal wurtzite CdS and its standard powder diffraction card (PDF No. 41-1049) [9–12]. All composite patterns still contain the g-C_3N_4 (002) reflection. Its retention indicates that CdS incorporation causes no marked disruption of the layered g-C_3N_4 structure.

At 3% and 6% CdS, the patterns are dominated by g-C_3N_4. Weak CdS reflections at these loadings reflect the low content, small crystallites, and dispersion of CdS on the g-C_3N_4 surface. Increasing the loading to 9% and 12% makes the CdS peaks more distinct, as expected for a higher CdS phase content [4–6]. The CdS peaks at about 26.5° and 28.2° flank the g-C_3N_4 (002) peak near 27.4°. Their proximity may produce overlap or broadening in the region around 27°.

Both g-C_3N_4 and CdS reflections are present in the composites, and no obvious impurity peaks appear. The XRD patterns thus support phase coexistence and purity, with the basic crystal structures of both semiconductors retained. Determining whether the interface has type-II characteristics, or establishing a charge-migration direction, lies beyond XRD alone. Assessment requires XPS, band-edge, PL, and photoelectrochemical data [5,9–11,13].

3.2 SEM morphology and interfacial structure

Figure 3 compares SEM images of pure g-C_3N_4, pure CdS, and g-C_3N_4/CdS (9%, 140 °C). Stacked, wrinkled sheets with some aggregation are visible for g-C_3N_4 in Fig. 3a. Gas release, framework contraction, and restacking during thermal polymerization may produce this morphology. Pure CdS appears as aggregated nanoparticles or short crystallites in Fig. 3b. In the composite image (Fig. 3c), particles occupy the surfaces and edges of the g-C_3N_4 sheets, roughening their outlines. The particle–sheet morphology is consistent with CdS nucleation and deposition in situ during hydrothermal treatment.

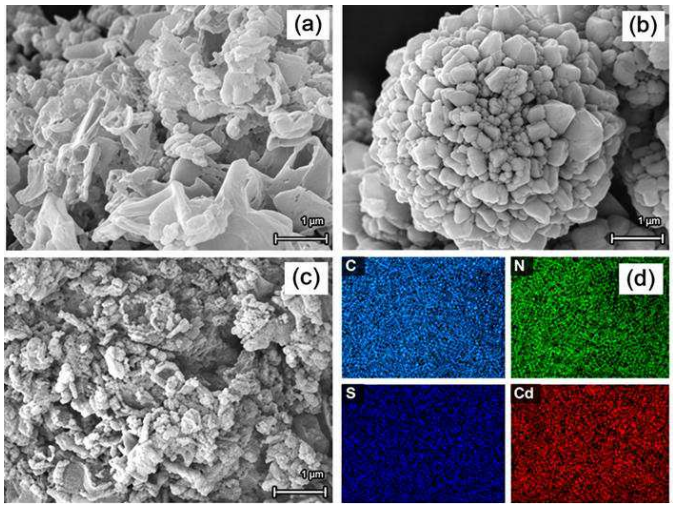

Fig. 3. SEM images of g-C_3N_4 (a), CdS (b), and g-C_3N_4/CdS (9%, 140 °C) (c), together with the C, N, S, and Cd elemental maps of the composite (d).

For the 9% composite, EDS detected C, N, Cd, and S in the spectrum shown in Supplementary Fig. S1. All four elements also extend across the mapped region in Fig. 3d. The Cd and S signals coincide spatially with the g-C_3N_4 substrate, supporting deposition of CdS on the sheets over simple

physical mixing of independent phases. This evidence is limited to elemental presence and co-location. Chemical valence, CdS stoichiometry, and interfacial charge-migration direction require XPS and band-structure measurements [5,10–11,13].

Among the different CdS loadings, the 9% sample shows relatively uniform particle dispersion and extensive particle–sheet contact. The g-C_3N_4 framework remains continuous, with CdS at multiple surface and edge sites and no apparent large aggregates. Such contact shortens interfacial transport paths while retaining accessible surface-reaction sites. Lower loadings provide fewer heterointerfaces. With further CdS addition, accumulation, sheet coverage, and local aggregation may instead lower the fraction of interfaces that contribute effectively.

The XRD and SEM observations describe different aspects of composite formation. Coexisting g-C_3N_4 and hexagonal CdS phases are evident in XRD, while SEM places CdS particles on the g-C_3N_4 sheets rather than in a separate, simply mixed powder. For the 9% sample, distinct CdS reflections accompany well-dispersed particles in contact with the sheets. Extensive contact is therefore achieved while the layered g-C_3N_4 framework remains intact. Earlier CdS/g-C_3N_4 studies have likewise used phase coexistence, uniform particle loading, and close contact to infer heterointerface formation [4–7,9–11,13].

Hydrothermal growth yields a two-phase material in which CdS is distributed relatively uniformly on g-C_3N_4 sheets, as indicated by SEM and XRD. The resulting interfacial contact provides the structural context for the XPS, UV–Vis DRS, PL, EIS, transient-photocurrent, and Mott–Schottky results. Distinguishing type-II from S-scheme charge migration requires the band-structure, electrochemical, and photoresponse evidence, since morphology and diffraction alone do not resolve the pathway. The main-text SEM images show the overall morphology and interfacial distribution. Supplementary Fig. S2 provides the higher-magnification images.

3.3 XPS analysis of surface chemical states

The XPS survey spectra in Fig. 4a are dominated by C 1s and N 1s for pure g-C_3N_4. In g-C_3N_4/CdS (9%), Cd 3d and S 2p are also present, with no unexpected elemental peaks, confirming CdS at the surface. The high-resolution Cd 3d spectrum (Fig. 4f) has peaks at 404.7 and 411.5 eV. Their separation of approximately 6.8 eV and assignments to Cd $3d_{5/2}$ and Cd $3d_{3/2}$ are consistent with Cd^{2+} in CdS. The S 2p peak near 161.1 eV in Fig. 4b corresponds to sulfide S^{2-}. A weak feature around 167.6 eV is more plausibly associated with surface-oxidized sulfur, adsorbates, or background contributions. Peak-area information and fitting constraints are unavailable, so this feature is not treated as primary evidence for lattice sulfur. The Cd^{2+} and S^{2-} assignments agree with those reported for CdS/g-C_3N_4 composites [4–5,14,16].

Compositing shifts the C 1s peaks from 284.8 and 288.0 eV in pure g-C_3N_4 to 285.0 and 288.2 eV, respectively (Fig. 4c). The 284.8–285.0 eV component is assigned to C–C/C=C or surface-carbon reference species. The component at 288.0–288.2 eV corresponds to N–C=N in the conjugated g-C_3N_4 framework. In Fig. 4d, the main N 1s peak moves from 398.6 to 398.7 eV. The satellite/excitation component at high binding energy, near 404 eV, shifts from 404.0 to 404.7 eV. Calibration and peak-fitting constraints affect these assignments [15]. Positive shifts in both C 1s and N 1s suggest reduced local electron density in g-C_3N_4 after contact with CdS, consistent with reported interfacial electron redistribution [5,14,17]. They do not, on their own, identify the photoinduced migration direction or distinguish type-II and S-scheme heterojunctions.

The O 1s feature shifts from 532.2 to 531.9 eV after compositing (Fig. 4e). Adsorbed oxygen, surface hydroxyl groups, or small amounts of oxygen-containing adsorbates offer a more reasonable assignment than lattice oxygen in CdS. When read alongside the two-phase XRD patterns and particle–sheet contact in SEM, XPS supports interfacial electronic coupling in the composite. The chemical-state information informs the subsequent assessment of band alignment and carrier transport using UV–Vis DRS, Mott–Schottky, PL, EIS, and transient photocurrent. Identifying the heterojunction type still requires the band-structure and photoelectrochemical evidence to be considered together [10,14–16].

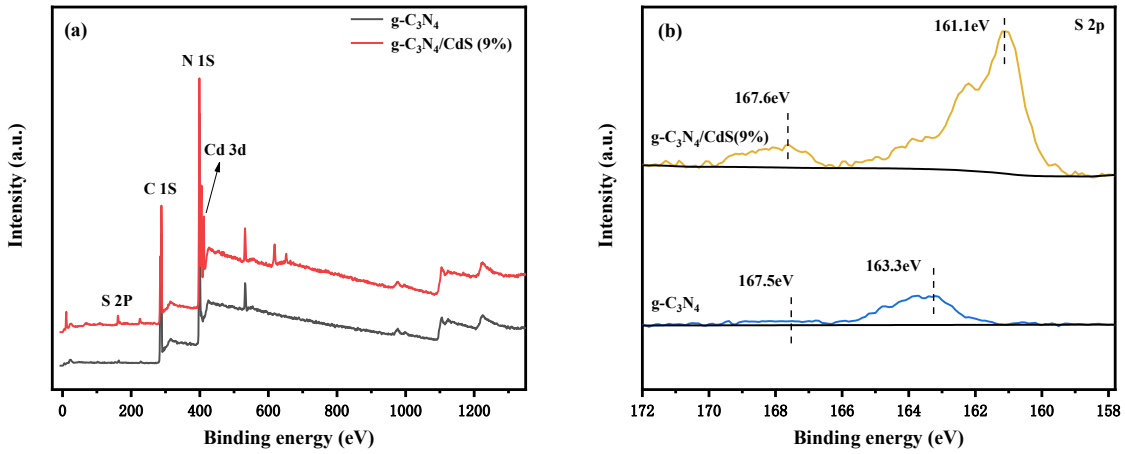

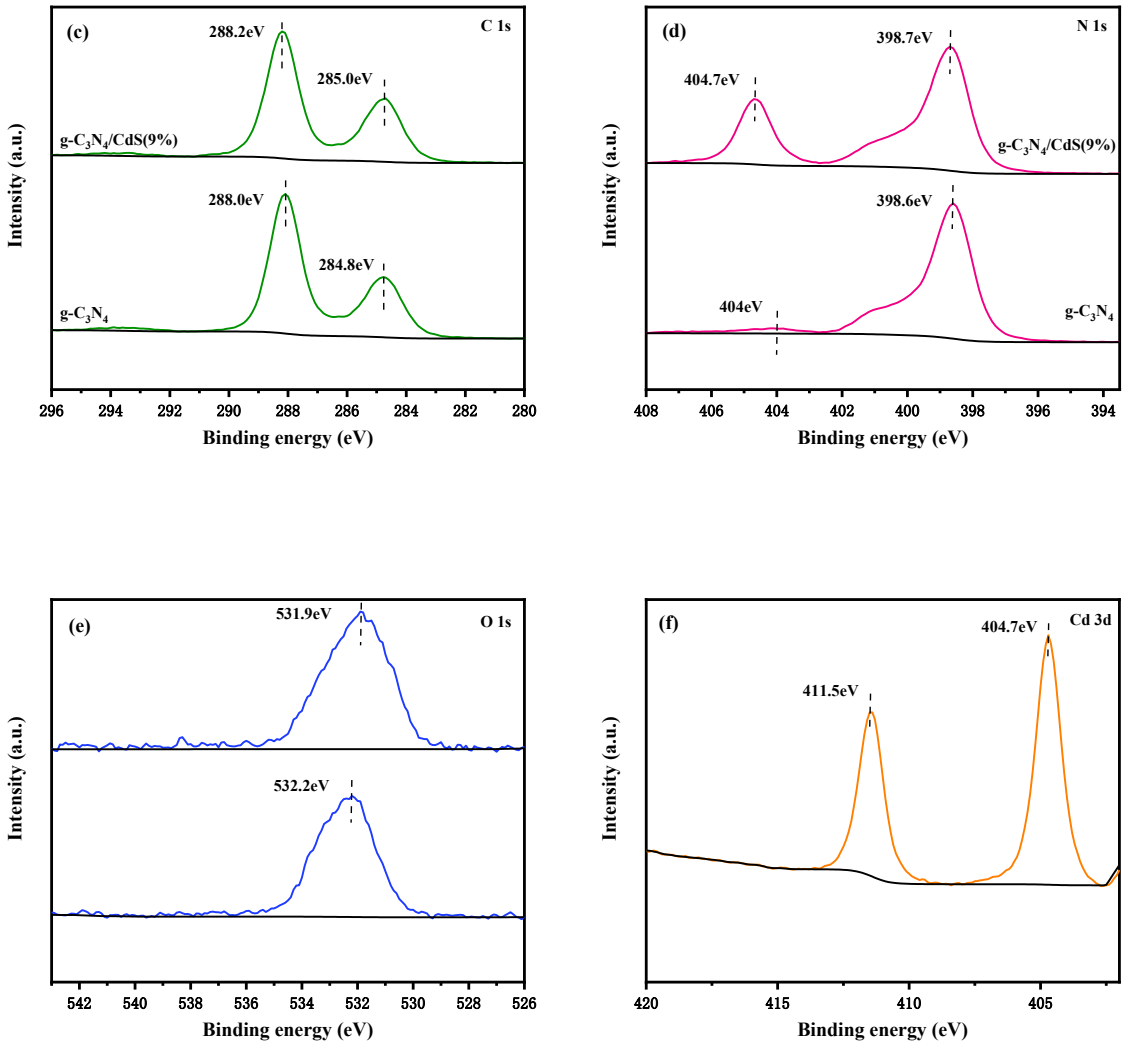

Fig. 4. (a) XPS survey spectra of the g-C_3N_4, and g-C_3N_4/CdS (9%, 140 °C) , and the corresponding high-resolution spectra of (b) S 2p, (c) C 1s , (d) N 1s, (e) O 1s, (f) Cd 3d.

3.4 UV–Vis absorption and optical band-gap analysis

UV–Vis spectra in Fig. 5 compare the absorption of pure g-C_3N_4, pure CdS, and the composites across the CdS-loading series. The g-C_3N_4 absorption edge lies at approximately 450–500 nm and mainly reflects π–π* transitions in its conjugated framework. With its narrower optical band gap, CdS absorbs across a broader visible-light range and extends to longer wavelengths. The 3%, 6%, 9%, and 12% composites retain the main g-C_3N_4 features but absorb more strongly over an extended visible-light range. The two semiconductors thus provide complementary optical responses. Similar redshifts and broadening in CdS/g-C_3N_4 have been attributed to CdS loading and electronic changes at closely contacted heterointerfaces [27–28].

The absorption range and intensity change with CdS content, although the dependence is nonlinear. Relatively strong absorption between approximately 300 and 500 nm and a continuous

visible-light response are retained in the 9% sample. The 12% sample absorbs more strongly in part of the longer-wavelength region, but that alone does not establish more efficient carrier use. Moderate loading disperses light-absorbing CdS domains over the g-C_3N_4 sheets and supplies interfacial contact. Low loading changes the optical response only slightly, whereas excessive CdS can obstruct effective light penetration through accumulation, shielding, or local absorption saturation. Optical band gaps were compared by Tauc extrapolation using the supplementary plots. Their interpretation should follow absorption-edge shifts as well as the plots, rather than absorbance at an isolated wavelength. Joint effects of CdS content, interfacial contact, and defect states on absorption edges and band gaps have also been reported [29–31].

Although CdS broadens the absorption of g-C_3N_4/CdS into the visible region, the 9% sample does not have the highest absorbance at every wavelength. It retains the principal g-C_3N_4 absorption features and a continuous visible-light response, with an optical band gap suited to its composite structure. This combination supports visible-light excitation within a loading range that improves light response before excessive shielding becomes detrimental. Neither absorption spectra nor band-gap estimates independently establish how carriers migrate. Reports on other CdS/carbon-nitride systems have described comparable interfacial coupling and cooperative band-gap modulation [32].

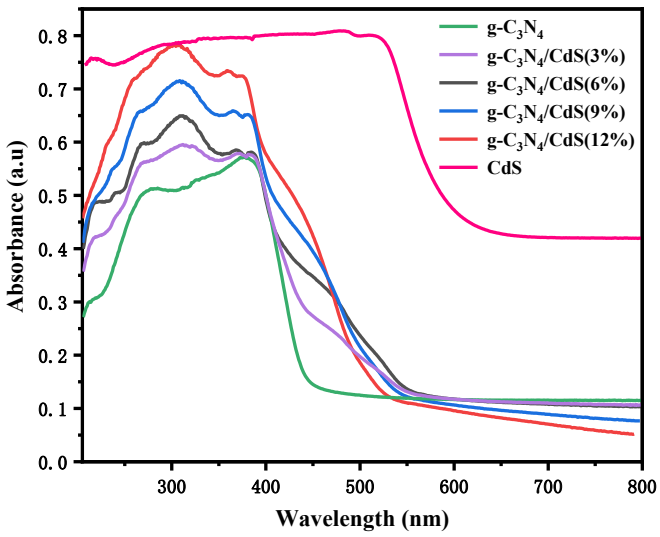

Fig. 5. UV–Vis absorption spectra of g-C_3N_4, CdS, and g-C_3N_4/CdS composites with different CdS proportions.

3.5 Photoluminescence analysis

The strong emission band of pure g-C_3N_4 at approximately 450–500 nm in Fig. 6 is associated with radiative electron–hole recombination. PL intensities decrease markedly in all four composites containing 3%, 6%, 9%, and 12% CdS. This quenching indicates suppression of radiative recombination upon CdS/g-C_3N_4 contact. It can reflect interfacial charge transfer or increased nonradiative deactivation, so the electron-migration direction cannot be inferred from PL alone. EIS, transient photocurrent, and band-structure data provide the complementary evidence needed for interpretation [10,14,16–17].

The lowest PL intensity occurs at 9% CdS, where carrier recombination is most strongly suppressed. Effective heterointerfaces are less abundant at 3% and 6%. Raising the CdS content to 12% increases PL again, indicating that charge separation does not improve continuously with loading. Particle accumulation, additional interfacial defects, or newly available recombination paths may explain the increase. The 9% response fits the relatively uniform dispersion in SEM, clear phase coexistence in XRD, and electron redistribution inferred from XPS. Together, these observations favor a composition that supplies interfacial contact while limiting recombination associated with aggregation and defects.

For the 9% composite, strong PL quenching supports reduced radiative recombination and a larger carrier population available to photocatalytic reactions. PL covers only the radiative contribution to recombination. Charge transport was therefore also examined by EIS, transient photocurrent, and CV.

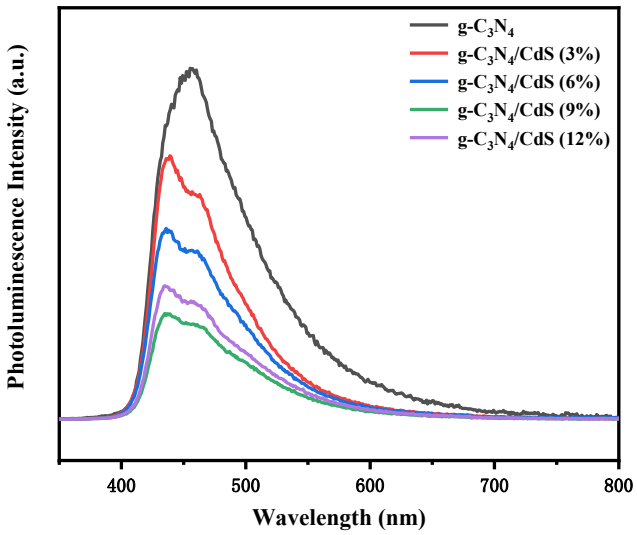

Fig. 6. PL spectra of g-C_3N_4 and the 3%, 6%, 9%, and 12% g-C_3N_4/CdS composites.

3.6 Transient photocurrent response

Switching the light on produced a rapid positive-current rise in every sample in Fig. 7; switching it off returned the current close to the dark baseline. These repeated responses indicate that photogenerated carriers can be extracted at the electrode interface. Pure g-C_3N_4 gave approximately 3 μA cm^{-2}. Incorporating 3% and 6% CdS increased the response to about 8 and 15 μA cm^{-2}, respectively, consistent with improved generation and interfacial extraction of carriers. The peaks permit a comparison of effective carrier output in this measurement configuration. They are not direct measurements of absolute carrier-separation efficiency inside the material.

The largest photoresponse was measured for g-C_3N_4/CdS (9%). Its initial light-on peak reached approximately 25–26 μA cm^{-2}, followed by a steady response of about 20–23 μA cm^{-2}. Peak shape and recovery to the baseline remained fairly consistent over successive light on/off cycles. The stable response indicates high effective carrier output and comparatively small transport losses between the material and electrode interface. Relative to the lower loadings, 9% CdS supplies more effective heterointerfaces and more continuous electronic contact. This interpretation is restricted to the measured photocurrent amplitude and repeatability in the present test configuration [33–35].

Increasing CdS beyond 9% did not increase photocurrent. Despite its higher CdS content, the 12% sample gave a weaker response, showing that extractable current does not scale with CdS amount. The peak current, steady plateau, and return to the dark baseline in Fig. 7 favor the 9% composition. At this loading, light-absorbing domains, interfacial contact, and continuous transport paths appear suitably balanced. Additional CdS may accumulate particles, shield light locally, or introduce interfacial defects and thereby increase transport losses. High transient output and repeatable cycling account for the advantage of the 9% sample [36–37].

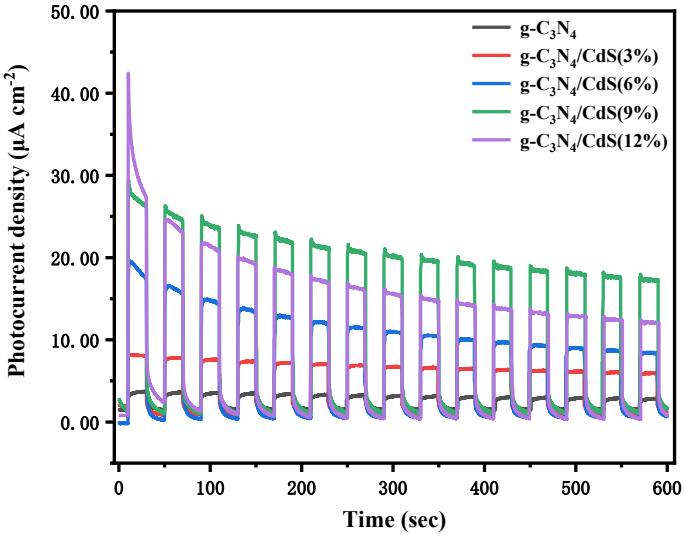

Fig. 7. Transient photocurrent responses of g-C_3N_4 and the 3%, 6%, 9%, and 12% g-C_3N_4/CdS composites.

3.7 Electrochemical impedance spectroscopy

Figure 8 presents the EIS Nyquist plots used to compare interfacial charge transfer in pure g-C_3N_4 and the composites. The high-frequency arc radius provides a qualitative indication of resistance at the electrode/electrolyte interface. Smaller arcs generally indicate lower charge-transfer resistance and faster transport. Every composite had a smaller arc than pure g-C_3N_4, supporting improved charge transfer across CdS–g-C_3N_4 interfaces. These responses depend on the measurement conditions, however, and cannot directly quantify carrier-separation efficiency.

The smallest EIS arc was obtained at 9% CdS. This sample therefore had the lowest apparent charge-transfer resistance and the most favorable migration across the composite/electrode interface. A balance between dispersion, interfacial contact, and continuous transport paths may account for the response. Fewer effective heterointerfaces limit transport at low loadings. At 12%, aggregation, less direct pathways, and additional charge-trapping defects may raise the impedance. The 9% arc supports improved interfacial transfer following heterojunction formation, while quantitative comparison would require equivalent-circuit fitting and replicate measurements [38–42].

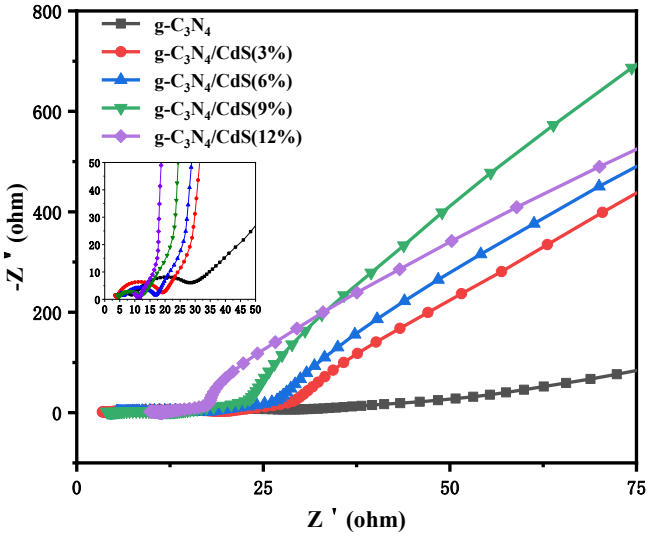

Fig. 8. EIS Nyquist plots and enlarged high-frequency region for g-C_3N_4 and g-C_3N_4/CdS composites with different CdS proportions.

3.8 Cyclic voltammetry and electrochemical response

In Fig. 9a, CV curves of g-C_3N_4/CdS (9%) recorded at 70 mV s^{-1} cover 100 consecutive cycles in darkness and under illumination. Light increased the anodic plateau from approximately 0.30–0.33 to 0.47–0.50 mA cm^{-2}. Little distortion or attenuation appeared over 100 cycles, suggesting enhanced interfacial charge exchange under illumination and good electrochemical stability. The dark curves in Fig. 9b compare pure g-C_3N_4 with the loading series. All composites enclosed larger areas and gave higher currents than g-C_3N_4. At approximately 0.75 mA cm^{-2}, the current density of the 9% sample clearly exceeded those of the 3% and 6% samples, consistent with more extensive CdS/g-C_3N_4 contact.

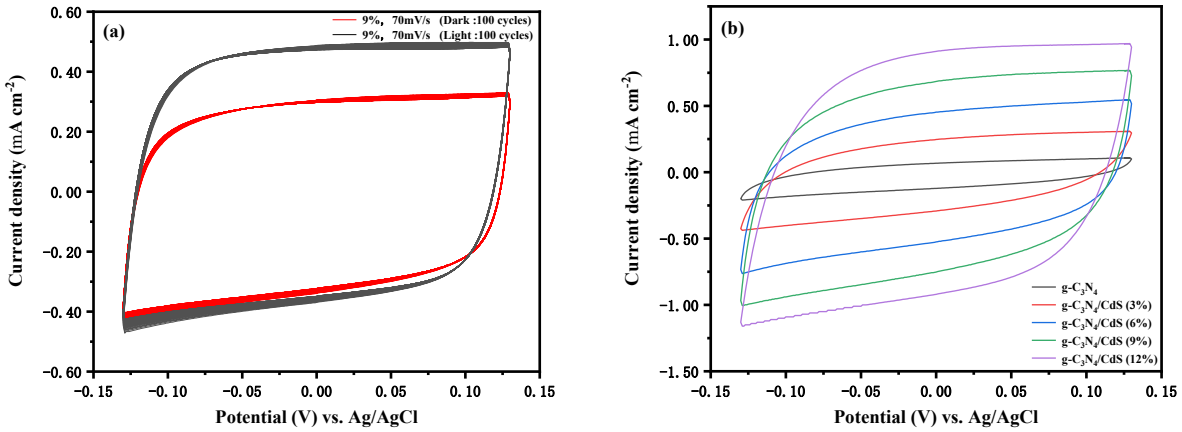

Fig. 9. (a) CV curves of g-C_3N_4/CdS (9%, 140 °C) over 100 consecutive cycles in the dark , and (b) dark CV curves of pure g-C_3N_4 and composites with different CdS proportions at the same scan rate.

The 12% sample enclosed a larger CV area and gave a higher current than the 9% sample. This response indicates greater apparent polarizability or interfacial charge-storage capacity without establishing higher photocatalytic activity. Film thickness, particle packing, double-layer charging, and effective surface area also affect CV. For the 9% composite, the highest transient photocurrent and weakest PL emission favor a balance between charge response, photocarrier use, and structural dispersion. Figure 10c shows an approximately linear current response with scan rate over 10 to 90 mV s^{-1}. The fit in Fig. 10b gives $R^2 \approx 0.99983$ and a double-layer capacitance of approximately 0.996 mF cm^{-2}, supporting stable interfacial polarization and substantial apparent charge storage. Double-layer capacitance does not directly measure true specific surface area or replace a photocatalytic activity measurement. Considered with XRD, SEM, XPS, PL, and photocurrent, the CV results support favorable contact and charge exchange at 9% CdS [4,10,14,16–17].

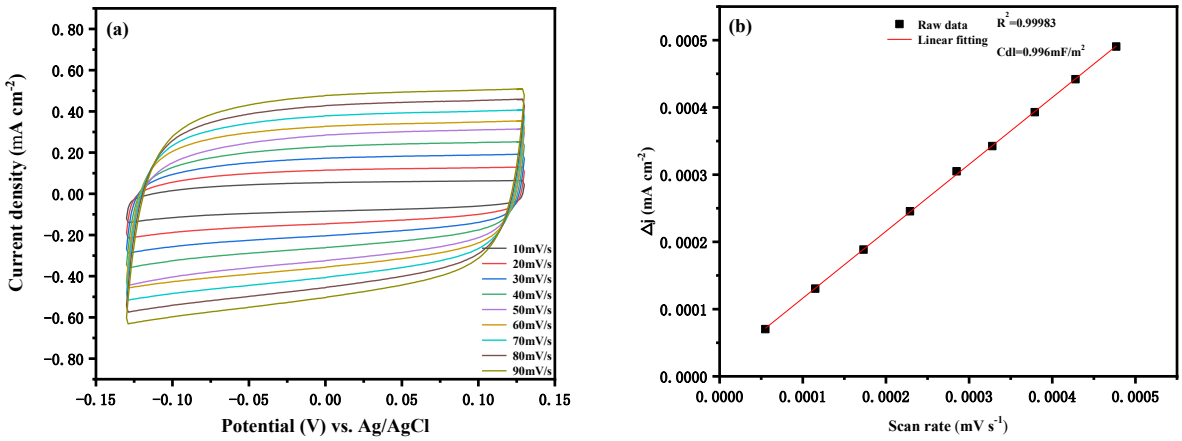

Fig. 10. (c) CV curves of g-C_3N_4/CdS (9%, 140 °C) at scan rates of 10–90 mV s^{-1} and (b) a linear fit of current response versus scan rate.

Supplementary reporting of scan-rate-dependent currents, peak-to-peak potential separations, and standard deviations across replicate electrodes could help distinguish double-layer capacitance from Faradaic contributions. Within the available measurements, the 9% sample shows a relatively stable interfacial charge response.

3.9 Mott–Schottky analysis and band structure

Positive slopes are observed for pure g-C_3N_4, pure CdS, and g-C_3N_4/CdS (9%) in the Mott–Schottky plots of Fig. 11, indicating n-type behavior. Extrapolating the linear regions gives flat-band potentials of approximately −0.95 V for g-C_3N_4, −0.76 V for the composite, and −0.42 V for CdS. These values follow the Ag/AgCl reference-electrode scale in the figure. The flat-band potential can approximate the conduction-band edge in an n-type semiconductor, although

reference-electrode calibration, test pH, carrier density, and other conditions affect the exact conversion. The present values are used for relative band-position comparisons, with no claim that they directly measure absolute band energies [10,14].

The flat-band potential falls between those of the pure components for the 9% composite. This intermediate position supports electronic rearrangement upon contact and agrees with the XPS core-level shifts and UV–Vis band-gap changes. Combined with the supplementary band-gap plots, the potentials allow approximate conduction- and valence-band positions to be considered. They also permit assessment of whether the alignment supports visible-light excitation and selective interfacial migration. Band matching is thermodynamically supported by Mott–Schottky intercepts and optical gaps, but these measurements cannot alone select a type-II or S-scheme pathway. XPS, PL quenching, EIS, and transient photocurrent remain necessary parts of the assessment [4–5,10,14,16–17].

For the 9% sample, a suitable relative conduction-band position accompanies strong visible-light response and effective interfacial charge separation. Its PL intensity is the lowest, its transient photocurrent the highest, and its impedance response substantially better than that of pure g-C_3N_4. The combined observations suggest changes in band structure and interfacial potential that provide a more favorable route for photogenerated carriers at 9% CdS. These measurements inform the interpretation of TCH degradation, pH effects, and reactive species. Assigning specific reaction pathways still requires the degradation kinetics and scavenger results.

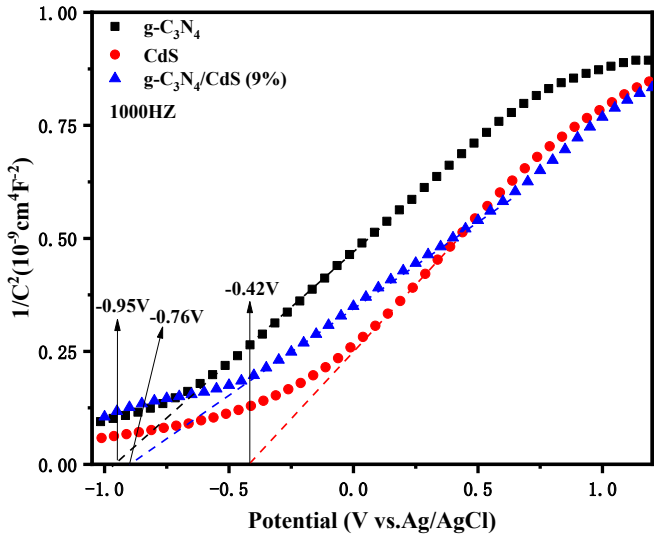

Fig. 11. Mott–Schottky plots of g-C_3N_4, CdS, and g-C_3N_4/CdS (9%, 140 °C).

3.10 Photocatalytic degradation performance

Degradation tests covered CdS loading, hydrothermal synthesis temperature, initial TCH concentration, solution pH, reuse, and reactive-species scavengers. The comparisons led to selection of g-C_3N_4/CdS (9%, 140 °C) for the subsequent experiments. In the curves, the initial dark period corresponds to adsorption–desorption equilibration, followed by photocatalytic degradation during illumination. Apparent kinetic parameters were fitted with a pseudo-first-order model. UV–Vis spectra at different TCH concentrations established the characteristic wavelength used to measure concentration. The spectra and peak assignment are provided in Supplementary Fig. S3.

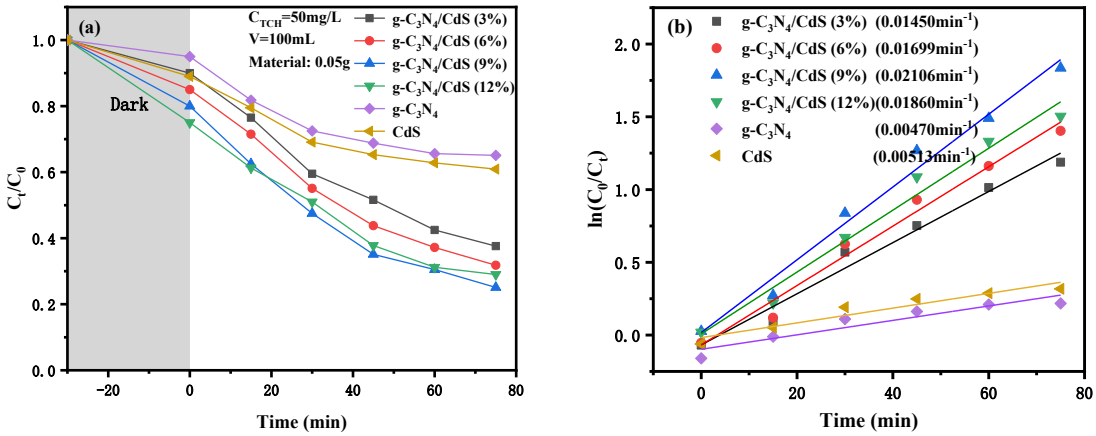

Fig. 12. (a) TCH degradation curves and (b) corresponding apparent kinetic fits for samples with different CdS proportions.

Under illumination, g-C_3N_4/CdS (9%) removed TCH most rapidly in the loading comparison (Fig. 12a). Dark adsorption had already lowered C_t/C_0 to different extents across the samples, and all continued to remove TCH after illumination began. For the 9% composite, C_t/C_0 reached approximately 0.25 after 75 min, equivalent to about 75% degradation. The pseudo-first-order fits in Fig. 12b give 0.02106 min^{-1} for this sample. The corresponding constants are 0.01450, 0.01699, and 0.01860 min^{-1} for the 3%, 6%, and 12% composites, and 0.00470 and 0.00513 min^{-1} for pure g-C_3N_4 and pure CdS. The 9% sample thus exceeds both the other loadings and the pure components. XRD, SEM, XPS, PL, and photocurrent indicate a distinct two-phase structure, relatively uniform particle–sheet contact, interfacial electron redistribution, and improved separation. These features favor adsorption, carrier transport, and surface redox reactions. Below 9%, effective heterointerfaces and useful photocarriers remain limited. At 12%, accumulation, shielding, and additional defects may offset the gain in CdS content. An intermediate optimum is consistent with reported interface optimization in g-C_3N_4/CdS for TCH degradation [4,6,10].

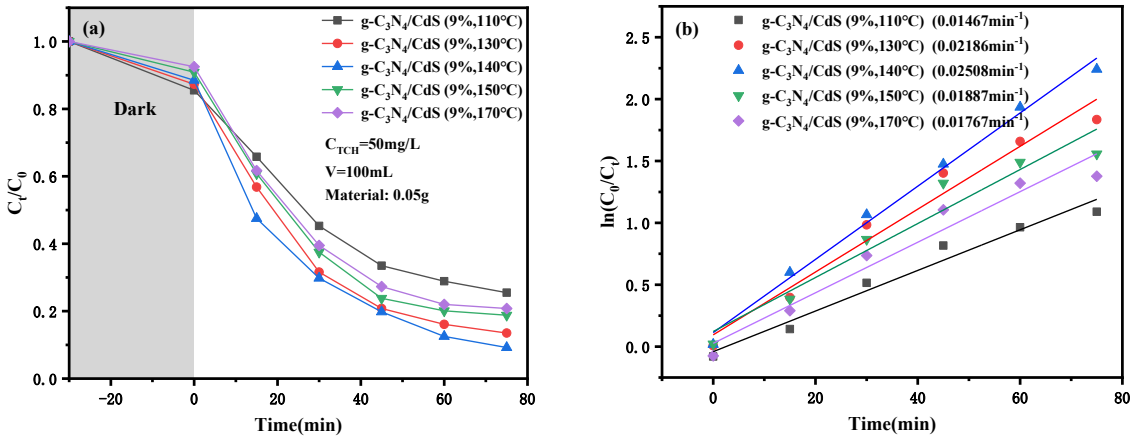

Fig. 13. (a) TCH degradation curves and (b) apparent kinetic fits for 9% g-C_3N_4/CdS samples prepared at different hydrothermal temperatures.

Hydrothermal temperature produced a volcano-shaped variation in the rate of TCH degradation by the 9% composites (Fig. 13). Samples prepared at 110, 130, 140, 150, and 170 °C gave apparent constants of 0.01467, 0.02186, 0.02508, 0.01887, and 0.01767 min^{-1}, respectively. The curves in Fig. 13a and fits in Fig. 13b both favor 140 °C, which yielded the lowest illuminated C_t/C_0 and highest rate constant. This response points to the most favorable interface for reaction within the tested series. Raising the temperature can promote CdS nucleation, crystallization, and contact with g-C_3N_4. Further heating may enlarge crystallites, aggregate particles locally, or reconstruct interfacial defects, reducing effective contact. The optimum at 140 °C agrees with the weakest PL emission, highest photocurrent, and favorable charge-exchange response. Interfacial quality and carrier use therefore matter alongside CdS crystallinity. Comparable temperature windows have been linked to the balance between crystallite size, contact, and defect density in CdS/g-C_3N_4 heterostructures [4,6,18].

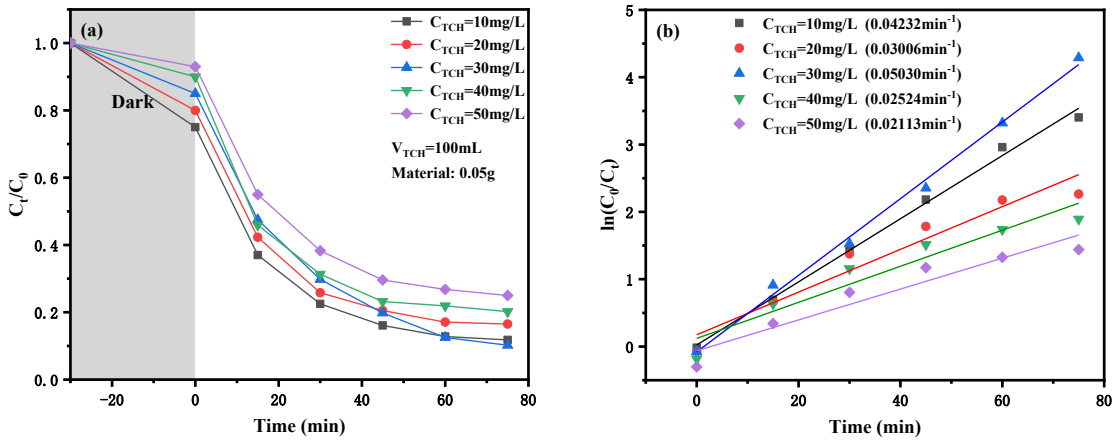

Fig. 14. (a) Degradation curves and (b) apparent kinetic fits for g-C_3N_4/CdS (9%, 140 °C) at different initial TCH concentrations.

The concentration series gave a nonmonotonic kinetic response (Fig. 14). For initial TCH concentrations of 10, 20, 30, 40, and 50 mg L^{-1}, the apparent constants were 0.04232, 0.03006, 0.05030, 0.02524, and 0.02113 min^{-1}, respectively. Changing concentration from 10 to 50 mg L^{-1} altered both normalized degradation and the fitted rate. The 30 mg L^{-1} run had the steepest fit in Fig. 14b and among the lowest final C_t/C_0 values in Fig. 14a. It was therefore chosen for cycling and scavenger tests. Initial concentration changes pollutant loading and surface coverage while also affecting light penetration and competition for active sites. At high concentrations, shielding by TCH and occupation of surface sites can lower the redox flux available per molecule. At low concentrations, sparse adsorption coverage or a short fitting interval may make the results more sensitive to sampling error. For this 9% composite, 30 mg L^{-1} balances mass transfer, absorption, and interfacial reaction favorably. Prior work has similarly related concentration effects to light shielding, active-site competition, and surface-reaction kinetics [3,6].

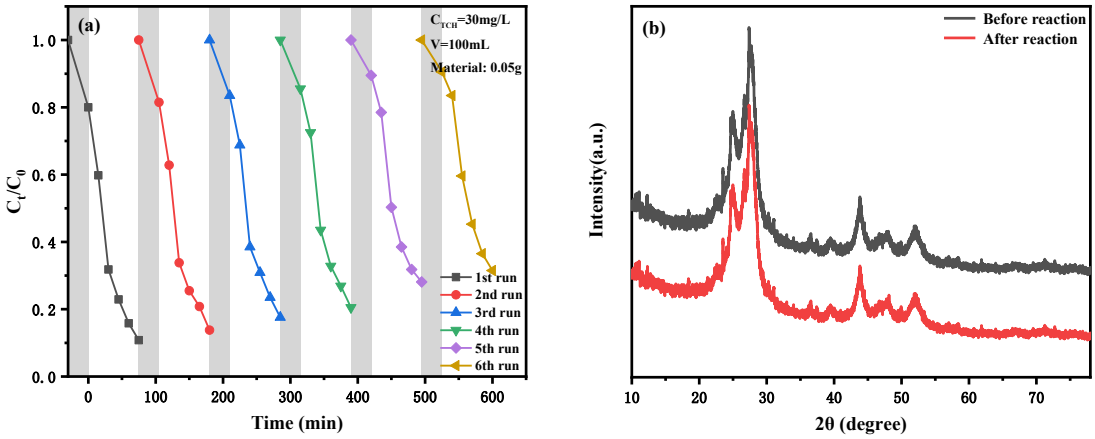

Fig. 15 (a) Cycling degradation curves for g-C_3N_4/CdS (9%, 140 °C) at 30 mg L^{-1} TCH and XRD patterns before and (b) after repeated degradation.

Six consecutive TCH degradation cycles tested the stability and reusability of g-C_3N_4/CdS (9%, 140 °C). Concentration declined in every cycle (Fig. 15a), indicating that active sites remained after recovery and reuse. Later cycles ended at higher concentrations, however, revealing a gradual loss of apparent activity. Before- and after-use XRD patterns in Fig. 15b retain the g-C_3N_4 and hexagonal wurtzite CdS peaks at essentially unchanged positions, without obvious new impurity reflections. There is thus no evidence of marked bulk phase transition or decomposition during reuse. Reduced peak intensities are more plausibly explained by recovery losses, adsorbate coverage, microstrain, or preferred orientation than by direct damage to the CdS lattice. Recycling losses and surface-state changes are therefore more likely explanations for the activity decline than obvious phase instability. Retained cycling activity and nearly unchanged post-reaction peak positions have also supported structural-stability interpretations in other CdS composites [22–23]. Supplementary peak positions, full widths at half maximum, relative intensities, recovered masses, and mass-normalized constants would help distinguish material loss from intrinsic deactivation.

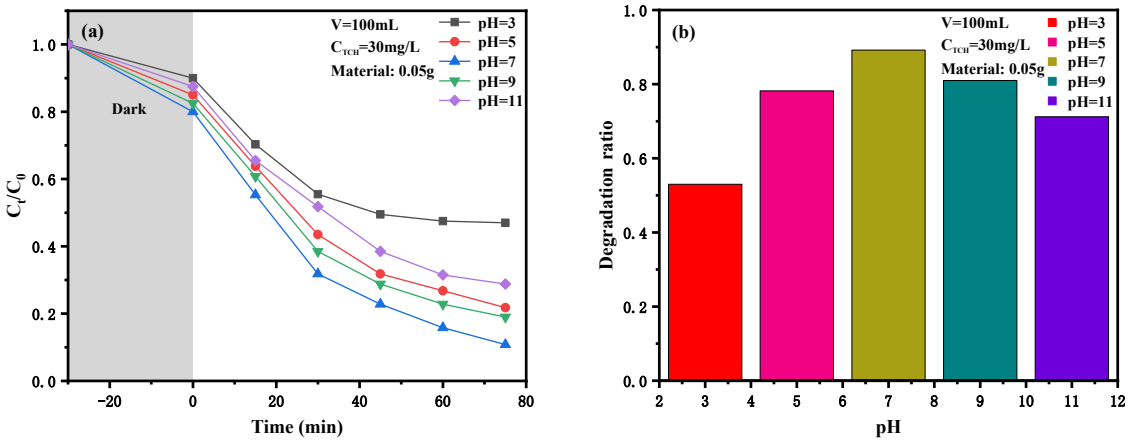

Fig. 17. (a) TCH degradation curves and (b) degradation efficiencies of g-C_3N_4/CdS (9%, 140 °C) at different initial pH values.

The highest TCH degradation efficiency occurred at pH 7 in Fig. 17. At pH 3, 5, 7, 9, and 11, the efficiencies were approximately 0.53, 0.78, 0.89, 0.81, and 0.71, respectively. Figure 17a shows the degradation curves and Fig. 17b compares efficiencies. Strongly acidic conditions gave the lowest removal. Solution pH changes TCH protonation/deprotonation, surface hydroxylation, and interfacial charge distribution together. Acidic protonation of the catalyst surface may weaken TCH adsorption and electron transfer. At high pH, anionic TCH becomes more abundant, OH^- competes for adsorption sites, and CdS surface charge changes, potentially reducing reactant–site compatibility. The neutral-pH optimum consequently reflects TCH speciation, adsorption, and photocarrier reactions in combination. A single electrostatic interaction is insufficient to explain it. The results also indicate that the charge-separation advantage at 9% CdS persists in near-neutral water.

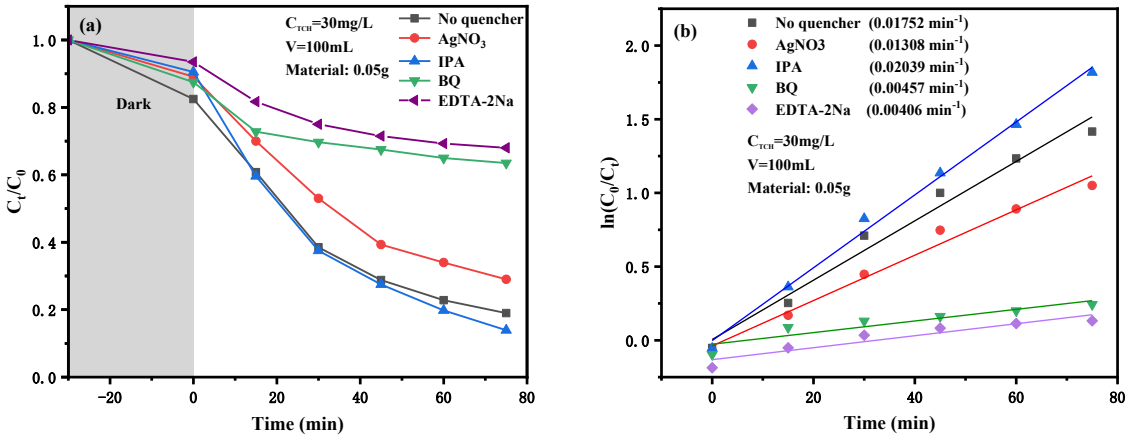

Fig. 16. (a) TCH degradation curves and (b) kinetic fits for g-C_3N_4/CdS (9%, 140 °C) in the presence of different scavengers.

BQ and EDTA-2Na produced the strongest inhibition in the scavenger tests (Fig. 16). The apparent constant was 0.01752 min^{-1} without a scavenger and fell to 0.00457 and 0.00406 min^{-1} with benzoquinone (BQ) and EDTA-2Na, respectively. $AgNO_3$ gave 0.01308 min^{-1}, while isopropanol (IPA) gave 0.02039 min^{-1}. Degradation curves and kinetic fits appear in Fig. 16a and Fig. 16b. BQ is commonly used to scavenge $\cdot O_2^-$ and EDTA-2Na to quench h^+, so their strong effects identify these species as major contributors to TCH degradation. $AgNO_3$ traps electrons; its moderate inhibition supports electron participation. IPA probes ·OH, and the absence of additional inhibition indicates that ·OH does not control the rate under these conditions. This interpretation fits the relatively negative conduction band, enhanced photocurrent, and weak PL of the 9% composite. Interfacial electrons can reduce O_2 to $\cdot O_2^-$, while holes can oxidize adsorbed TCH or surface water/hydroxyl species. Scavengers can also change pH, absorbance, and adsorption. Their effects are therefore considered with band positions and photoresponse, without assigning a unique pathway from scavenging alone.

Across the six photocatalytic comparisons, g-C_3N_4/CdS (9%, 140 °C) gave the best overall balance of loading, preparation temperature, concentration, pH, and repeated-use behavior. Its apparent rate was at or near the highest among the compared conditions. High normalized removal was obtained at 30 mg L^{-1} and pH 7, and a repeatable photocatalytic response remained during cycling. Scavenging identified $\cdot O_2^-$ and h^+ as the main reactive species. Phase coexistence and particle–sheet contact, together with the broader visible-light response and improved separation, are consistent with these degradation results.

3.11 Proposed photocatalytic degradation mechanism

Figure 18 presents a possible TCH degradation mechanism for g-C_3N_4/CdS (9%, 140 °C), drawing on XRD, SEM, EDS, XPS, UV–Vis, PL, transient-photocurrent, EIS, CV, Mott–Schottky, and scavenger measurements.

Visible light excites both g-C_3N_4 and CdS to generate electron–hole pairs. A model with type-II interfacial charge separation is consistent with the Mott–Schottky, optical band-gap, XPS, and photoelectrochemical results. In this model, electrons move from the g-C_3N_4 conduction band to that of CdS, while holes move from the CdS valence band to that of g-C_3N_4. Spatial separation suppresses recombination within each component. The higher transient photocurrent, smaller EIS arc, and stronger interfacial response at 9% loading also support a more effective transport route [10,24–26]. Band gaps and Mott–Schottky measurements mainly test compatibility of band positions, however, and cannot establish a unique migration pathway. The type-II description is accordingly proposed as a model that fits the available evidence and is evaluated together with the scavenger results.

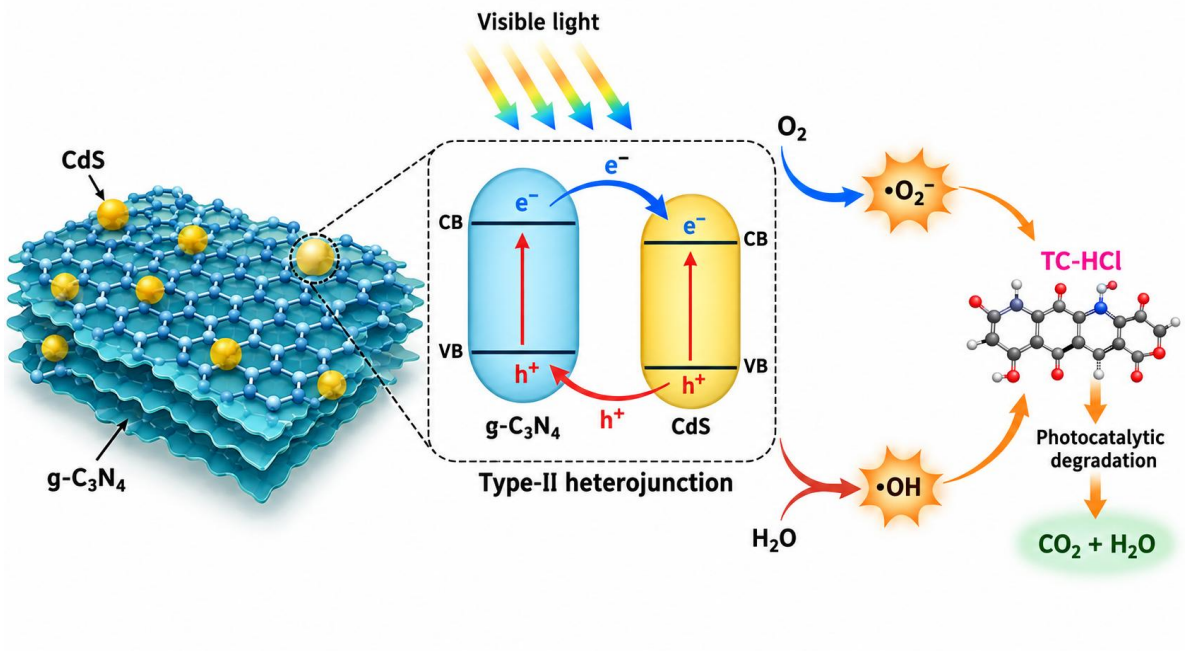

Fig. 18. Proposed mechanism for photocatalytic degradation of TCH over g-C_3N_4/CdS (9%, 140 °C).

Electrons reaching the interface can preferentially reduce dissolved oxygen. Holes can oxidize adsorbed TCH directly or react with surface water and hydroxyl species. Strong decreases in the apparent rate after adding BQ and EDTA-2Na indicate major roles for $\cdot O_2^-$ and h^+, respectively. Moderate inhibition by $AgNO_3$ supports electron involvement in oxygen reduction. IPA caused no clear further inhibition, indicating that ·OH is not the principal rate-limiting species under these

conditions. The reactions below therefore depict $\cdot O_2^-$ and h^+ as the main oxidation pathways and retain ·OH as a possible secondary species.

$$g\text{-}C_3N_4/CdS + h\nu \rightarrow g\text{-}C_3N_4/CdS\ (e^- + h^+) \quad (2)$$

$$e^- + O_2 \rightarrow \cdot O_2^- \quad (3)$$

$$h^+ + TCH \rightarrow TCH^{\cdot +} \rightarrow \text{oxidation intermediates} \quad (4)$$

$$h^+ + H_2O \rightarrow \cdot OH + H^+ \quad (5)$$

$$h^+ + OH^- \rightarrow \cdot OH \quad (6)$$

$$\cdot O_2^- + TCH \rightarrow \text{oxidation intermediates} \quad (7)$$

$$\text{Oxidation intermediates} + \cdot O_2^-/h^+ \rightarrow CO_2 + H_2O\ \text{(possible pathway toward extensive oxidation)} \quad (8)$$

Adsorption first brings TCH onto the g-C_3N_4/CdS surface. Attack by $\cdot O_2^-$ and h^+, with a smaller contribution from ·OH, may disrupt aromatic conjugation and cleave nitrogen-containing groups and side chains. Hydroxylation, dealkylation, and ring opening can then yield progressively smaller intermediates. Figure 18 includes CO_2 and H_2O as possible endpoints after extensive oxidation. These transformations and the route to complete mineralization remain inferred from reactive-species and photoelectrochemical evidence: neither TOC nor LC–MS was measured to verify them directly. The highest efficiency at pH 7 also supports favorable matching of TCH speciation, surface state, and carrier-mediated reactions in neutral solution. The charge-separation benefit of the 9% sample may therefore remain useful under conditions approaching actual water environments.

The activity increase in g-C_3N_4/CdS (9%, 140 °C) may result from visible-light excitation of both components followed by spatial separation and migration at a type-II-like interface. Surface redox reactions are then driven by electrons in the CdS conduction band and holes in the g-C_3N_4 valence band. Scavenger results assign the main roles to $\cdot O_2^-$ and h^+ and an auxiliary role to ·OH.

Moderate CdS content supplies heterointerfaces and light absorption while leaving active sites accessible, matching the optimum found in the loading and synthesis-temperature tests.

4. CONCLUSIONS

One-step high-temperature calcination produced g-C_3N_4, on which CdS was grown hydrothermally at different nominal proportions. Both the g-C_3N_4 and hexagonal wurtzite CdS phases remained in the composites, with no obvious impurity phase in XRD. SEM and EDS placed CdS particles on the g-C_3N_4 sheets. The 9% sample showed relatively uniform particle–sheet contact and extensive interfacial coupling. CdS broadened visible-light response and altered the interfacial chemical environment and electronic structure. The weakest PL emission, highest transient photocurrent, and smallest EIS arc were obtained for g-C_3N_4/CdS (9%), indicating a favorable balance of contact, transport, and recombination loss. Its apparent TCH degradation constant was 0.02106 min^{-1}, exceeding those of the other loadings and pure g-C_3N_4 and CdS. Temperature optimization increased the constant to 0.02508 min^{-1} for the 140 °C sample. This optimum was attributed to an intact, closely contacted heterointerface with relatively low charge-transfer resistance. Degradation remained repeatable through cycling, and the principal crystalline phases were largely retained. Removal was greatest at pH 7, consistent with favorable matching of TCH speciation, surface state, and photogenerated-carrier reactions in neutral solution. Scavenging identified $\cdot O_2^-$ and h^+ as the principal reactive species, with ·OH contributing secondarily. The improved photocatalytic behavior is associated with cooperative excitation, interfacial charge separation, and electron- and hole-driven surface redox reactions. The results support g-C_3N_4/CdS composites for photocatalytic treatment of antibiotic-containing wastewater.

ASSOCIATED CONTENT

Supporting Information

The Supporting Information is available free of charge.

EDS spectrum of g-C_3N_4/CdS (9%, 140℃); high-magnification SEM images of g-C_3N_4, CdS, and g-C_3N_4/CdS (9%, 140℃); and UV-vis absorption spectra of tetracycline hydrochloride solutions at different concentrations.

STATEMENTS AND DECLARATIONS

Funding

This work was supported by the Key Research and Development Program of Shaanxi Province (Grant No. 2026CY-YBXM-797) and the National Natural Science Foundation of China (Grant No. 12204295).

Data Availability

The data generated or analyzed during this study are available from the corresponding author upon reasonable request.

REFERENCES

[1] L. Jiang, W. Zhai, J. Wang, et al. Antibiotics and antibiotic resistance genes in the water sources of the Wuhan stretch of the Yangtze River. Environmental Research, 2023, 239: 117295.

[2] H. Zheng, Y. Ji, S. Li, et al. Ecotoxicity and resistance genes induction changing of antibiotic tetracycline degradation products dominated by differential free radicals. Environmental Research, 2023, 227: 115427.

[3] Z. Xu, J. Nie, G. Mao, et al. Engineering dual carbon and nitrogen vacancies in g-C_3N_4 for enhanced photodegradation of tetracycline hydrochloride. Langmuir, 2024, 40: 23051 – 23059.

[4] S. Jing, J. Zhao, A. Wang, et al. Efficient photocatalytic production of H_2O_2 and photodegradation of tetracycline by CdS/square tubular g-C_3N_4 S-scheme heterojunction photocatalyst. Chemical Engineering Journal, 2024, 479: 147150.

[5] B. Feng, L. Wu, A. Jv, et al. Accurate construction of Cd/CdS/g-C_3N_4 heterojunction interface for efficient photocatalytic tetracycline degradation and Cr(VI) reduction. Colloids and Surfaces A, 2024, 701: 134981.

[6] W. Zhang, H. Liu, Z. Chen, et al. In situ construction of CdS/g-C3N4 heterojunctions in spent thiolation@wood-aerogel for efficient excitation peroxymonosulfate to degradation tetracycline. ACS Applied Materials & Interfaces, 2024, 16: 28353 – 28366.

[7] E.V. Siddhardhan, A. Steephen, et al. Efficient removal of TC and CIP antibiotics by surface modified g-C_3N_4/CdS nanocomposite under sunlight irradiation. Dyes and Pigments, 2024, 225: 112052.

[8] W.J. Ong, L.L. Tan, Y.H. Ng, et al. Graphitic carbon nitride (g-C_3N_4)-based photocatalysts for artificial photosynthesis and environmental remediation. Chemical Reviews, 2016, 116: 7159 – 7329.

[9] G.K. Valencia, A. Hernández Gordillo, L. Cerezo, S.E. Rodil. Blue light hydrogen production via CdS/g-C_3N_4 heterojunctions. Dalton Transactions, 2025, 54: 8483 – 8497.

[10] M. Saad, A. Bahadur, S. Iqbal, et al. Development of stable S-scheme 2D – 2D g-C_3N_4/CdS nanoheterojunction arrays. Scientific Reports, 2024, 14: 2897.

[11] X. Cong, A. Li, F. Guo, et al. Construction of CdS@g-C_3N_4 heterojunction photocatalyst for highly efficient degradation of gaseous toluene. Science of the Total Environment, 2024, 913: 169777.

[12] Z.-Y. Wang, L. Xu, C.-H. Liu, et al. MXene/CdS photothermal – photocatalytic hydrogels for efficient solar water evaporation and synergistic degradation of VOC. Journal of Materials Chemistry A, 2024, 12: 10991 – 11003.

[13] P. Wang, X. Han, X. Zheng, et al. Removal of tetracycline hydrochloride by photocatalysis using electrospun PAN nanofibrous membranes coated with g-C_3N_4/Ti_3C_2/Ag_3PO_4. Molecules, 2023, 28: 2647.

[14] X. Zhang, et al. Band Alignment Tuning via the Facets of CdS Nanocrystals with g-C_3N_4 for Unveiling Their Enhanced Photocatalytical Property. Advanced Functional Materials, 2024.

[15] S. Blechert, et al. Can X-ray Photoelectron Spectroscopy Characterize Photocatalytically Relevant Defects in Graphitic Carbon Nitride? Re-examining Peak Assignment and Quantification Using Model Compounds. Chemistry of Materials, 2024, 36: 9762 – 9774.

[16] R. Sun, et al. Rapid charge migration of hierarchical S-Scheme g-C_3N_4/CdS@C for efficient photocatalytic hydrogen evolution. International Journal of Hydrogen Energy, 2024, 55: 635 – 644.

[17] S. Singh, R.K. Yadav, S.Y. Choi, et al. Enhancing Photocatalytic CO_2 Reduction and Photo-oxidative Coupling over CdS/S-g-C_3N_4 Heterojunction Interface into Solar Chemicals. Energy & Fuels, 2025, 39: 1746 – 1758.

[18] F. Wu, X. Chen, J. Han, L. Zhao, W. Wang. Degradation of tetracycline hydrochloride by semi-embedded CdS/tubular g-C_3N_4 heterojunction photocatalysts loaded with Ni nanoparticles. New Journal of Chemistry, 2024, 48: 11327 – 11337.

[19] K. Wannakan, S. Nonthing, A. Panchakeaw, S. Nanan. Fe2O3/g-C_3N_4/CdS photocatalysts for complete sunlight-active detoxification of the tetracycline antibiotic and Congo red dye in water. RSC Advances, 2025, 15: 42867 – 42886.

[20] Z. Meng, Z. Peng, Y. Yan, Q. Zhang, Y. Li. Non-radical degradation mechanism on ZnO quantum dots/hollow-sphere g-C_3N_4 S-scheme heterojunction photocatalysts for tetracycline degradation. iScience, 2025, 28(10): 113500.

[21] L. Wang, X. Wang, X. Xu, F. Wu, Y. Ge. Construction of ZnO quantum dots anchored in oxygen-doped g-C_3N_4: A novel Z-type heterojunction with boosting photocatalytic performance for tetracycline degradation. Journal of Molecular Structure, 2025, 1328: 141382.

[22] Y. Zhou, K. Liu, S. Zhuang, Y. Mu. GO/CdS heterojunctions for accelerated photocatalytic antibiotic degradation. Nanomaterials, 2025, 15(19): 1475.

[23] X. Chen, F. Wu, J. Han, et al. Enhanced photocatalytic degradation of tetracycline hydrochloride over Cd-CdS@g-C_3N_4 under visible light irradiation. Materials Today Communications, 2024, 39: 108496.

[24] X. Duan, J. Yang, J. Zhu, et al. Activated CdS/sulfur doped g-C_3N_4 photocatalyst for dye and antibiotic degradation: Experimental and DFT verification of S-scheme heterojunction. Environmental Research, 2025, 266: 120487.

[25] D. Wang, Y. Ai, M. Liu, et al. Visible-light driven carbon dots modulating Z-scheme g-C_3N_4/CdZnS heterojunction for efficient photocatalytic degradation of tetracycline. Journal of Photochemistry and Photobiology A: Chemistry, 2025, 116894.

[26] X. Hu, Z. Zhang, P. Lu, et al. Cyano-deficient g-C_3N_4 for round-the-clock photocatalytic degradation of tetracycline: Mechanism and application prospect evaluation. Water Research, 2024, 260: 121936.

[27] Y. Niu, J. Shen, W. Guo, et al. The synergistic effect in CdS/g-C_3N_4 nanoheterojunctions improves visible light photocatalytic performance for hydrogen evolution reactions. Molecules, 2023, 28(17): 6412.

[28] L. Ma, W. Jiang, C. Lin, et al. CdS deposited in situ on g-C3N4 via a modified chemical bath deposition method to improve photocatalytic hydrogen production. Molecules, 2023, 28(23): 7846.

[29] Y. Lin, Z. Chen, C. Feng, et al. Preparation of S-C_3N_4/AgCdS Z-scheme heterojunction photocatalyst and its effectively improved photocatalytic performance. Molecules, 2024, 29(9): 1931.

[30] M. Shoaib, M.Y. Naz, S. Shukrullah, et al. Dual S-scheme heterojunction CdS/TiO_2/g-C_3N_4 photocatalyst for hydrogen production and dye degradation applications. ACS Omega, 2023, 8(45): 43139 − 43150.

[31] A. Banu, B. Sinha, S. Sikdar. Synthesis of polymeric 2D-graphitic carbon nitride (g-C_3N_4) nanosheets for sustainable photodegradation of organic pollutants. Heliyon, 2024, 10(13): e33354.

[32] Q. Lv, H. Lu, X. Wang, et al. Photocatalysis over CdS quantum dots/oxygen doped g-C_3N_4 Z-scheme heterojunction: Revealing the synergistic effects of quantum confinement effect, defect engineering, and Z-scheme mechanism. Chemical Engineering Journal, 2025, 524: 169496.

[33] J. Lee, Y. Lee, J. Yu, K. Yim, A.N. Kadam, S.-W. Lee. Interface engineered cascade-type electronic structure of 2D/0D/2D CdS − $CdCO_3$/SnO_2 quantum dots/g-C_3N_4 nanocomposite for boosting solar-driven photocatalysis. Environmental Research, 2024, 256: 119202.

[34] J. Wang, H. Huo, G. Sui, S. Meng, D. Guo, S. Fu, D. Zhang, X. Yang, J. Li. Rational design of a g-C_3N_4/CdS/MIL-125(Ti)-derived TiO_2 ternary heterojunction as a highly efficient photocatalyst for wastewater treatment under visible-light irradiation. Sustainable Energy & Fuels, 2024, 8: 2889.

[35] J. Pei, H. Li, D. Yu, D. Zhang. g-C_3N_4-based heterojunction for enhanced photocatalytic performance: A review of fabrications, applications, and perspectives. Catalysts, 2024, 14(11): 825.

[36] S. Das, L.W. Ng, C. Chong, V. Pereira, H. Li, C.-L.K. Lee, H.K. Lee. Effective interfacing of surface homojunctions on chemically identical g-C_3N_4 for efficient visible-light photocatalysis without sacrificial agents. Small, 2024, 20(33): e2400780.

[37] N. Khan, G. Burashev, A. Kadylbekova, et al. Sustainable scalable solid-state synthesis of highly efficient synergetic 2D/0D micro/nanostructured g-C_3N_4/CdS photocatalysts for hydrogen production and water purification. Sustainable Materials and Technologies, 2024, 41: e01063.

[38] M. Joseph, B. Meena, R. Joy, S. Joseph, R.K. Sethi, S.N. Remello, S. Haridas, C. Subrahmanyam. Rational design of a g-C_3N_4/Bi_2S_3/ZnS ternary heterojunction photoanode for improved solar water splitting. Sustainable Energy & Fuels, 2024, 8: 3412 – 3418.

[39] E.K. Feyie, E.A. Zereffa, A. Tadesse, M. Goddatti, D. Noh, E. Oh, L.T. Tufa, J. Lee. An efficient p – n heterojunction copper tin sulfide/g-C_3N_4 nanocomposite for methyl orange photodegradation. ACS Omega, 2024, 9(26): 28463 – 28475.

[40] Y. Chen, et al. Intense interaction between biochar/g-C_3N_4 promotes the photocatalytic performance of heterojunction catalysts. RSC Advances, 2024, 14: 18864 – 18876.

[41] M. Ismael, et al. Progress on g-C_3N_4 based heterojunction photocatalyst for H_2 production via photocatalytic water splitting. Journal of Alloys and Compounds, 2024, 1002: 175062.

[42] R.R. Salunkhe, et al. Recent advances of graphitic carbon nitride (g-C_3N_4) based materials for photocatalytic applications: A review. Nano Materials Science, 2024.

Supplementary Files

This is a list of supplementary files associated with this preprint. Click to download.

- AssociatedContent.docx